communications chemistry

ARTICLE

https://doi.org/10.1038/s42004-023-00978-3 OPEN

Ion solvation as a predictor of lanthanide adsorption structures and energetics in alumina nanopores

Anastasia G. Ilgen [1✉], Nadine Kabengi[2], Jacob G. Smith[1] & Kadie M. M. Sanchez[1]

Adsorption reactions at solid-water interfaces define elemental fate and transport and enable contaminant clean-up, water purification, and chemical separations. For nanoparticles and nanopores, nanoconfinement may lead to unexpected and hard-to-predict products and energetics of adsorption, compared to analogous unconfined surfaces. Here we use X-ray absorption fine structure spectroscopy and *operando* flow microcalorimetry to determine nanoconfinement effects on the energetics and local coordination environment of trivalent lanthanides adsorbed on Al_2O_3 surfaces. We show that the nanoconfinement effects on adsorption become more pronounced as the hydration free energy, ΔG_{hydr}, of a lanthanide decreases. Neodymium (Nd^{3+}) has the least exothermic ΔG_{hydr} ($-3336\ kJ{\cdot}mol^{-1}$) and forms mostly outer-sphere complexes on unconfined Al_2O_3 surfaces but shifts to inner-sphere complexes within the 4 nm Al_2O_3 pores. Lutetium (Lu^{3+}) has the most exothermic ΔG_{hydr} ($-3589\ kJ{\cdot}mol^{-1}$) and forms inner-sphere adsorption complexes regardless of whether Al_2O_3 surfaces are nanoconfined. Importantly, the energetics of adsorption is exothermic in nanopores only, and becomes endothermic with increasing surface coverage. Changes to the energetics and products of adsorption in nanopores are ion-specific, even within chemically similar trivalent lanthanide series, and can be predicted by considering the hydration energies of adsorbing ions.

[1] Geochemistry Department, Sandia National Laboratories, 1515 Eubank Boulevard SE, Albuquerque, NM 87123, USA. [2] Department of Geosciences, Georgia State University, 24 Peachtree Center Avenue NE, Atlanta, GA 30303, USA. ✉email: agilgen@sandia.gov

Adsorption reactions at solid-water interfaces are relevant to ion-selective capture[1–7], chemical separations[8–11], catalysis[6], and environmental fate and transport[12–14]. When solid surfaces are nanoconfined (for nanoparticles or inside nanopores), their apparent reactivity starts being influenced by the surface energy terms, which become significant at the nanoscale[6,15–18]. Importantly, inside nanopores filled with aqueous solutions electrical double-layers (EDL) extending from the charged surfaces may overlap, causing the structures of nanoconfined solutions to differ from those observed at unconfined surfaces. Nanoconfined water has a lower dielectric response[19–24], and lower density and surface tension[25], defined by the H-bonding structures[16,26] and slower rotational dynamics in near-interfacial regions[27,28]. Despite much information about nanoconfined water, the reactivities of nanoconfined surfaces, including the pathways and products of adsorption reactions, are not easily predicted[15,17,18,29–33]. This uncertainty is because adsorption in nanoconfined systems is dictated by both surface chemistry (e.g., the density of Si–OH, Al–OH, or other functional groups[17,18,30,31] and charge distribution[34]) as well as the size of the pore/channel that determines the solute structures within the overlapping EDLs. These interdependent effects have hindered the discovery of reliable predictors for how the energetics, pathways, and products of adsorption reactions change under nanoconfinement[12,13,29,30]. Here we show that the hydration energy of an adsorbing ion (ΔG_{hydr}) could be used as a meaningful predictor.

Previous studies have reported that nanoconfinement enhances inner-sphere adsorption and shifts the net adsorption heat from exo- (unconfined) to endothermic (nanoconfined) for cation adsorption onto negatively-charged silica (SiO_2) surfaces and on zeolites[15,29,30,32,35]. Ilgen et al. concluded that the adsorption of cations with less exothermic (less negative) ΔG_{hydr} is affected more by nanoconfinement compared to cations with more exothermic ΔG_{hydr} and tighter hydration shells[29]. This trend was observed for the products and heats of adsorption for SiO_2 surfaces nanoconfined within pores under 7 nm in diameter[29]. Therefore, the ΔG_{hydr} of an ion could be used to anticipate the extent of nanoconfinement effects on its adsorption behavior. However, this trend has only been shown thus far for negatively-charged SiO_2 surfaces[29]. Here we study lanthanide adsorption on positively-charged alumina (Al_2O_3) surfaces and present further evidence that ΔG_{hydr} is in fact a reliable predictor of nanoconfinement effects on adsorption.

To test our hypothesis that *ΔG_{hydr} controls whether cation adsorption energetics and products are affected by nanoconfinement*, we exploit the gradual change in the ΔG_{hydr} of trivalent lanthanide cations (Ln^{3+}) and compare their adsorption on unconfined Al_2O_3 (*i.e.*, corundum) and Al_2O_3 surfaces nanoconfined within 4.4 nm pores. Using *operando* flow microcalorimetry we show that at low surface coverages, adsorption reaction is endothermic for unconfined Al_2O_3 and becomes exothermic when Al_2O_3 surfaces are nanoconfined; adsorption becomes more endothermic as surface coverage is increased. Using X-ray absorption fine structure (XAFS) spectroscopy, we show that local structures around adsorbed neodymium (Nd^{3+}) are vastly different for corundum and nanoconfined Al_2O_3 surface, while they are virtually indistinguishable on both surfaces for the stronger-hydrated lutetium (Lu^{3+}). To our knowledge, this is the first study of lanthanide adsorption on nanoconfined Al_2O_3 surfaces that describes interfacial structures together with adsorption energetics.

Accurate molecular-scale descriptions of nanoconfined Al_2O_3 surface reactivities are crucial for predictive models of contaminant mobilities, immobilization of radionuclides within heterogeneous nuclear wastes, and water purification with Al_2O_3 membranes[36]. Al_2O_3 is a building block of soils and rocks, therefore it can drive macroscopic chemical fluxes in the environment[12,13,37]. Furthermore, understanding structure-reactivity relationships for Ln^{3+} in nanoconfined systems can enable the separation of these critical elements using reactive nanopores[38]. The presented work illustrates that the energetics and products of adsorption could be predictably controlled by changing the size of a reactive nanopore.

Results and discussion

Adsorption complexes on corundum and nanoconfined Al_2O_3 surfaces. The local coordination environment of adsorbed Nd, Tb, and Lu on corundum and nanoconfined Al_2O_3 surfaces was characterized using XAFS. We found that nanoconfinement promotes inner-sphere adsorption for Nd^{3+} cations and causes subtle elongation of the Lu–O bonds for inner-sphere Lu complexes. There is a stark difference in the surface speciation of adsorbed Nd when compared to Lu: Lu forms inner-sphere complexes (chemisorption) on both corundum and nanoconfined Al_2O_3 surfaces. Nd, however, only forms outer-sphere complexes (physisorption) on corundum, and inner-sphere complexes on porous Al_2O_3 surfaces (Fig. 1). This conclusion is based on the Nd L_{III}-edge Fourier transformed XAFS spectrum for corundum Al_2O_3 having no detectable 2nd shell neighbor, while for Nd adsorbed onto nanoconfined Al_2O_3 surfaces the 2nd shell due to Nd-Al backscattering is well-resolved in the spectrum (Fig. 1). This observation supports our hypothesis that a cation's ΔG_{hydr} defines the extent to which nanoconfinement affects its adsorption products. In the examined set of cations, Nd^{3+} has the least exothermic ΔG_{hydr} ($-3336\ kJ{\cdot}mol^{-1}$)[39], and shows the most pronounced difference in the adsorption products when unconfined Al_2O_3 surfaces are compared to Al_2O_3 nanopores. On the other hand, Lu^{3+}, which has the most exothermic ΔG_{hydr} ($-3589\ kJ{\cdot}mol^{-1}$)[39], produces nearly identical XAFS spectra when corundum and nanoconfined Al_2O_3 surfaces are compared. All shell-by-shell fitting results for Nd, Tb, and Lu XAFS data are shown in Table 1. Raw data plotted in k-space with k-weight of 3 is shown in Fig. S1 in the Supporting Information file.

The 1st Nd–O shell for both corundum and nanoconfined Al_2O_3 surface was fit with a combination of two Nd–O theoretical backscattering paths at 2.45 ± 0.01 Å and 2.63 ± 0.01 Å (Table 1). The average Nd–O distance in these samples (2.54 Å) is similar to that reported for Nd^{3+} adsorbed onto SiO_2 surfaces nanoconfined within 4 nm to 7 nm pores[29]. The 2nd shell due to Nd-Al backscattering (observed only for nanoconfined Al_2O_3 surface) was fit with a Nd-Al theoretical path at 3.46 ± 0.05 Å, consistent with a bi-dentate bi-nuclear complex geometry.

For Tb, XAFS data was collected only for nanoconfined Al_2O_3 surfaces, where Tb forms inner-sphere surface complexes. The 1st Tb–O shell was fit with a combination of two Tb–O theoretical paths at 2.33 ± 0.01 Å and 2.46 ± 0.01 Å, again showing a similar local environment to that of Tb adsorbed onto SiO_2 surfaces nanoconfined within 4 nm and 7 nm SiO_2 pores[29]. The 2nd shell fits with a Tb-Al theoretical backscattering path at 3.4 ± 0.01 Å, which indicates a bi-dentate bi-nuclear surface complex geometry. XAFS data and fits for Tb, including fitting isolated 2nd shell, is shown in the Supporting Information file, Fig. S2. Similar to our earlier reported observations for Cu(II) and Ln(III) adsorbed on nanoconfined SiO_2 surfaces[29,30], dimerization reactions were evident for Tb and Lu on Al_2O_3: there is evidence of Tb-Tb and Lu-Lu backscattering contributions to the collected XAFS spectra. The presence of Tb–Tb backscattering suggests that some (not all) adsorbed Tb forms dimers or other types of polymeric species on nanoconfined Al_2O_3 surfaces; the Tb–Tb distance of

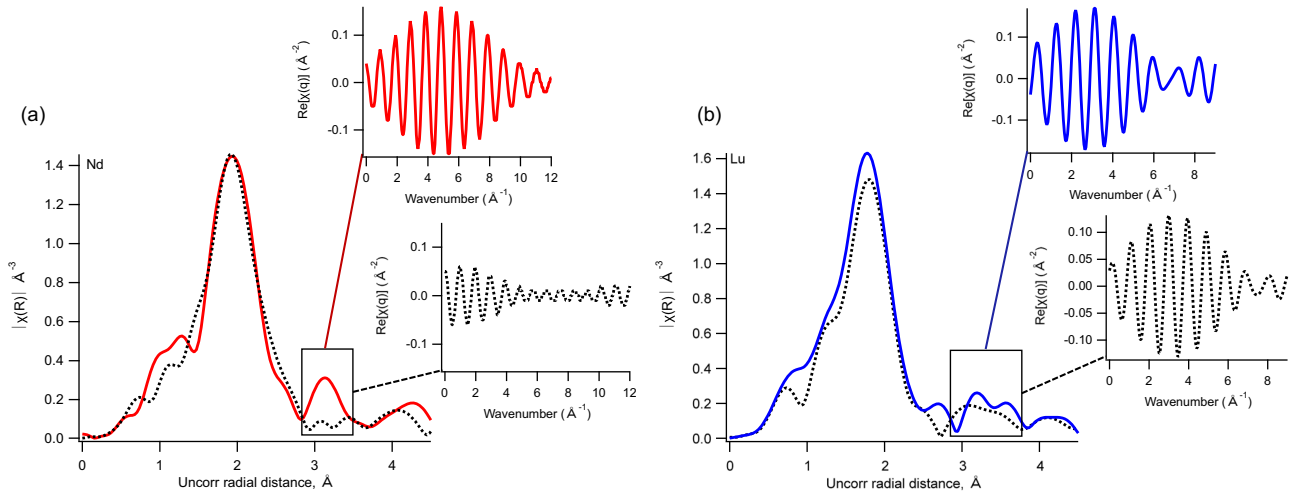

Fig. 1 X-ray absorption fine structure spectroscopy data for neodymium and lutetium adsorbed onto non-porous and porous alumina. X-ray absorption fine structure data for Nd (**a**) and Lu (**b**) adsorbed on corundum (dashed lines) and nanoconfined Al_2O_3 surfaces (solid lines); Fourier transform of each spectrum is shown. The insets in each panel illustrate back-transformed spectra of the isolated 2nd shell. For Nd, the 2nd shell is observed in the spectrum for the nanoconfined Al_2O_3 surface and corresponds to Nd-Al backscattering due to inner-sphere complexation; No 2nd shell is present for Nd adsorbed on corundum. For Lu, both spectra for corundum and nanoconfined Al_2O_3 are showing evidence for inner-sphere complexation.

Table 1 Summary of X-ray absorption fine structure (XAFS) spectroscopy shell-by-shell fitting results for Nd^{3+}, Tb^{3+}, and Lu^{3+} adsorbed onto corundum and nanoconfined Al_2O_3 with 4.4 nm pores.

Sample, coverage	[a]k-range	[a]R-range (Å)	Shell	[b]CN	[c]R (Å)	[d]σ^2 (Å^2)	[e]ΔE_0 eV	[f]R-factor	[g]Red χ^2	[h]Ind. Pts.
Nd-Al_2O_3- corundum, 13 mmol m^{-2}	2.6–10	1.5–3.8	Nd-O	5.4 ± 1.2	2.45 ± 0.01	0.001 ± 0.001	6.4 ± 1.2	0.011	4.3	11
			Nd-O	5.7 ± 1.0	2.63 ± 0.01	0.001 ± 0.001				
Nd-Al_2O_3-4 nm, 0.35 mmol m^{-2}	2.6–10	1.5–3.8	Nd-O	6.0 ± 0.6	2.46 ± 0.01	0.002 ± 0.001	5.9 ± 1.0	0.010	11	18
			Nd-O	5.2 ± 0.6	2.63 ± 0.01	0.003 ± 0.002				
			Nd-Al	1.8 ± 0.7	3.47 ± 0.05	0.002 ± 0.004				
Tb-Al_2O_3-4 nm, 0.48 mmol m^{-2}	2.6–10	1.5–4.0	Tb-O	6.4 ± 1.0	2.36 ± 0.01	0.002 ± 0.002	6.3 ± 1.6	0.012	126	19
			Tb-O	4.6 ± 1.2	2.50 ± 0.02	0.003 ± 0.003				
			Tb-Al	1.8 ± 1.0	3.38 ± 0.08	0.005 ± 0.018				
			Tb-Tb	1.6 ± 2	3.64 ± 0.2	0.011 ± 0.030				
Lu-Al_2O_3- corundum, 38 mmol m^{-2}	2.6–10	1.4–4.0	Lu-O	5 ± 1	2.22 ± 0.02	0.005 ± 0.002	7.5 ± 0.6	0.013	28	19
			Lu-O	4.9 ± 0.7	2.34 ± 0.01	0.003 ± 0.002				
			Lu-Al	4 ± 2	3.74 ± 0.06	0.006 ± 0.008				
			Lu-Lu	5 ± 4	3.88 ± 0.06	0.007 ± 0.008				
Lu-Al_2O_3-4 nm, 0.59 mmol m^{-2}	2.6–10	1.4–4.0	Lu-O	5.9 ± 0.4	2.26 ± 0.01	0.003 ± 0.001	6.5 ± 0.6	0.007	65	19
			Lu-O	4.4 ± 0.6	2.40 ± 0.02	0.003 ± 0.002				
			Lu-Al	3 ± 2	3.82 ± 0.06	0.009 ± 0.010				
			Lu-Lu	4 ± 4	3.92 ± 0.08	0.011 ± 0.010				

Fitting was done in R-space with simultaneous fitting of *k*-weights 1, 2, and 3. The amplitude reduction factor S_0 was set at 0.88 for Nd, 0.67 for Tb, and 0.71 for Lu, based on fitting XAFS spectra for model compounds Nd_2O_3, Tb_2O_3, and Lu_2O_3 with known structures. Errors at a 95% confidence level (2 sigma values) are shown.
[a]Usable *k*-range and *R*-range (uncorrected distances)
[b]Coordination number
[c]Bond length
[d]Debye-Waller factors: mean-square amplitude reduction factor, including thermal and static disorder components
[e]Energy shift between the theoretical and measured spectrum
[f]R-factor (mean square misfit) $R_{factor} = \frac{\sum_i (data_i - fit_i)^2}{\sum_i data_i^2}$
[g]Reduced chi-square $\chi^2_v = \frac{N_{idp}}{N_{pts}} \sum_i \left(\frac{data_i - fit_i}{\epsilon_i}\right)^2 / (N_{idp} - N_{var})$
[h]Independent points (number of data points minus the number of variable parameters) $N_{idp} = N_{pts} - N_{var}$

3.61 ± 0.06 Å suggests that the Tb polymerization is in the form of edge-sharing moieties (e.g., as in the structure of xenotime[40]).

Similar to Nd and Tb, two Lu–O backscattering paths were required to fit the 1st shell of the Lu spectra. For corundum, the Lu-O distances are 2.23 ± 0.02 Å and 2.34 ± 0.01 Å. For nanoconfined Al_2O_3 surfaces, the Lu-O distances are slightly longer, at 2.26 ± 0.01 Å and 2.41 ± 0.02 Å (Table 1). The elongation of the Lu-O distance under nanoconfinement may indicate that the local pH inside Al_2O_3 pores is lower than the controlled/measured pH of the adsorption reactor (6.0 ± 0.1). In our earlier publication, we show that for Lu adsorbed onto SiO_2 surface at pH 4.0 the Lu-O distances are ~0.1 Å longer, compared to an analogous sample at pH 6.0, likely due to the lower abundance of OH^- in the 1st shell around Lu at lower pH and shorter Lu-OH^- distances compared to the Lu-H_2O distance[29]. Recent studies indicate that inside SiO_2 nanopores protons are concentrated, driven by the negative surface charge inside nanopore[41]. However, Al_2O_3 surfaces are expected to be positively charged[42,43] at the near-neutral pH of

our experiments. Therefore, Lu-O elongation may be happening due to the EDL overlap and corresponding changes to the structure (hydrogen bonding) in nanoconfined water, rather than a higher proton concentration inside nanopores. The 2nd shell for Lu adsorbed onto corundum and nanoconfined Al_2O_3 surfaces was fit with Lu-Al theoretical backscattering path at 3.8 ± 0.06 Å, indicating a bi-dentate bi-nuclear adsorption complex, and additional Lu-Lu backscattering contribution indicating Lu dimers or other types of polymer surface species. The Lu–Lu distance of ~3.9 Å indicates a corner-sharing arrangement for Lu polyhedra (as we discuss in the previous publication[29], Lu-Lu edge-sharing would result in a shorter distance at ~3.55 Å, as in keiviite structure[44]). Similar to Lu adsorption on SiO_2, for Al_2O_3 we also observe bi-dentate complexation. On iron oxides, however, Lu tends to form mono-dentate complexes at pH 8 on hematite and at pH 5 on ferrihydrite[45].

Cation adsorption studies on nanoconfined Al_2O_3 surfaces are extremely limited and often lack spectroscopic analyses detailing surface speciation. On unconfined corundum surfaces uranium U(VI) likely adsorbs as outer-sphere complex because U(VI) adsorption was found to be both pH- and ionic-strength-dependent. However, on nanoconfined Al_2O_3 within ~1.3 nm pores U(VI) likely adsorbs as inner-sphere complexes since the adsorption is pH-dependent, while is independent of ionic strength[42]. These assumptions are also confirmed by sequential desorption experiments, where U(VI) shows irreversible adsorption onto nanoconfined Al_2O_3 and fully-reversible adsorption on corundum surfaces[42]. The most common U(VI) species at near-neutral pH is UO_2CO_3[46], for which ΔG_{hydr} was quantified at −41.17 kcal·mol^{-1} (−172.3 kJ·mol^{-1})[47]. The −172.3 kJ·mol^{-1} ΔG_{hydr} value for U(VI) is by far less favorable than that for Nd^{3+} (−3336 kJ·mol^{-1}); therefore macroscopically-observed differences in the U(VI) adsorption onto porous vs. non-porous Al_2O_3 agree with our predictions and observations for lanthanides.

Heats of Ln^{3+} adsorption quantified with *operando* flow microcalorimetry. Heats of Ln^{3+} adsorption on corundum and nanoconfined Al_2O_3 surfaces were quantified using *operando* flow microcalorimetry. At the conditions of these experiments, for all three Ln^{3+}, nanoconfinement reverses the enthalpic sign from an *endothermic* signal for the non-porous corundum to an *exothermic* signal on nanoconfined Al_2O_3 surfaces (Fig. 2). This finding is consistent with our previous investigations of Cu^{2+} and Ln^{3+} adsorption unto porous SiO_2 surfaces[29,30] whereby nanoconfinement resulted in a reversal of the enthalpic sign in the flow-through experiments. Additionally, *operando* flow microcalorimetry data can also point to the nature of surface complexes: e.g., the adsorption of Cr^{3+} as inner-sphere complexes is exothermic for SiO_2 (quartz) and corundum, while the adsorption of Al^{3+} on the same surfaces as outer-sphere complexes is endothermic[48].

In comparing the two Al_2O_3 surfaces, the adsorption of Ln^{3+} was significantly more energetic on nanoconfined Al_2O_3 surfaces than on corundum surfaces, potentially indicating enhanced inner-sphere complexation. The summary of the microcalorimetric results (Q_{ads} in mJ·m^{-2} and ΔH_{ads} in kJ·mol^{-1}) and surface coverages (in mol·m^{-2}) is shown in Table 2. The molar enthalpies, ΔH_{ads}, for Lu^{3+}, Tb^{3+}, and Nd^{3+} were calculated to be −34.8, −13.4 and −55.3 kJ·mol^{-1} on nanoconfined Al_2O_3 surfaces, and +1.77, +0.66, and +0.62 kJ.mol^{-1} on non-porous corundum surfaces, respectively. The largest difference between both surfaces was observed for Nd^{3+}, which is consistent with our XAFS data and our hypothesis that the lightest lanthanides with the least exothermic ΔG_{hydr} are affected more by nanoconfinement. It is crucial to note that no detectable calorimetric signal was detected at first for non-porous Al_2O_3, indicating that Q_{ads} was ~0 mJ·m^{-2}. To achieve a detectable calorimetric signal, the microcalorimetry experiments on non-porous Al_2O_3 were conducted at a higher Ln^{3+} concentration, resulting in higher surface coverages for non-porous corundum than for porous Al_2O_3. It is therefore possible that the overall higher energy measured for nanoconfined Al_2O_3 is disproportionately influenced by the high-energy sites, which are typically occupied first and can contribute more to the overall signal at lower surface coverages.

Enthalpy, entropy, and Gibbs Free energy of adsorption measured in temperature-controlled batch experiments. To assess the impact of surface coverage on the adsorption energetics we measured adsorption equilibrium constants in batch samples at temperatures ranging from 25 ± 1 °C to 45 ± 1 °C (298 K to 318 K). The surface coverages for all samples are provided in Table 2. In all batch reactors, the adsorbed Ln amount increases with increasing temperature, indicating endothermic adsorption for all Ln^{3+} cations on porous and non-porous Al_2O_3. The dataset used for thermodynamic calculations is included in the Supporting Information file (Table S1). While the calculated ΔH_{ads} values were positive for both solids, ΔS_{ads} values were negative for Al_2O_3 nanopores, and positive for corundum surfaces (Table 2). This result indicates a higher degree of freedom for species adsorbed onto the corundum surface and increased ordering of surface complexes inside nanopores. Due to these entropic effects, the calculated ΔG_{ads} values at room temperature are negative for corundum, indicating a spontaneous reaction, and positive for Al_2O_3 nanopores, indicating that adsorption is non-spontaneous.

When all batch and flow samples are considered, ΔH_{ads} values show a dependency on the surface coverage up to ~0.5 mmol m^{-2}, at which point mono-layer coverage is achieved (Table 2, Fig. 3). With increasing surface coverages ΔH_{ads} values become more endothermic. This finding is not surprising, as we noted above, since at lower surface coverages the adsorption predominantly occurs at high-energy sites; and with increasing surface coverage, lower energy sites become progressively occupied. All data from the batch and *operando* microcalorimetry experiments is summarized in Table 2 and plotted in Fig. 3 to illustrate this point.

Direct calorimetric measurements of adsorption enthalpies as a function of the amount adsorbed remain limited. However, using titration calorimetry, Machesky et al.[49] found that for the adsorption of iodate, fluoride, phosphate, and salicylate onto goethite, adsorption enthalpies become less exothermic as surface coverage increases, while at high surface coverages (>70%) even become endothermic for phosphate and fluoride. More recently Falaise et al.[50] observed variations of adsorption enthalpies with surface coverage for the sorption of Th^{4+}, $[UO_2]^{2+}$, and Nd^{3+} in a porous metal-organic framework, although each cation exhibited a different trend depending on its adsorption process.

Interpreting data on structure and energetics together. The overall free energy of adsorption is the sum of the electrostatic and chemical free energy changes (favorable to adsorption) and the solvation free energy change (unfavorable to adsorption)[51]:

$$\Delta G_{ads} = \Delta G_{coul} - \Delta G_{hydr} + \Delta G_{chem} \quad (1)$$

Consider electrostatic interactions (ΔG_{coul}) first: in our experiments, the Al_2O_3 surfaces are positively charged as they are in solutions at pH 6.0, which is below the reported point of zero charge (pH_{PZC}) values for various porous and non-porous

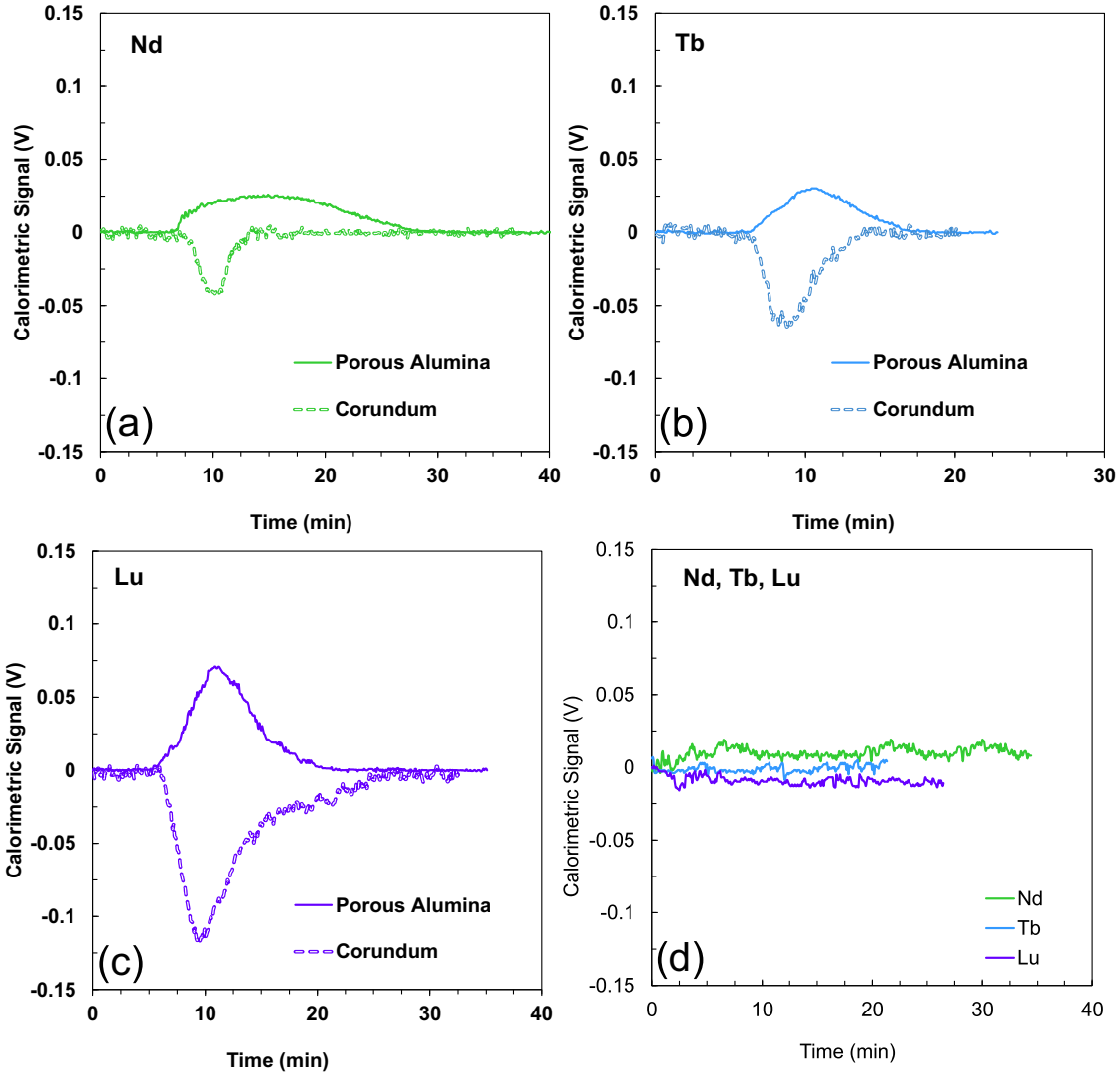

Fig. 2 *Operando* microcalorimetry data for neodymium, terbium, and lutetium adsorbing onto non-porous and porous alumina. Calorimetric signal obtained for the complexation of (**a**) Nd^{3+}, (**b**) $Tb^{3+}$and (**c**) Lu^{3+} on corundum and Al_2O_3 surfaces nanoconfined within 4 nm pores. An increase in voltage resulting in a positive peak corresponds to a release of energy and hence an exothermic reaction. For porous Al_2O_3, the concentrations were 7.86 μM for $Nd(NO_3)_3$, 11.22 μM for $Tb(NO_3)_3$ and 8.42 μM for $Lu(NO_3)_3$. Due to the low calorimetric signal obtained for corundum at the same aqueous concentrations (**d**), the concentrations of the stock solutions were increased to 157.2 μM for $Nd(NO_3)_3$, 224.4 μM for $Tb(NO_3)_3$, and 168.4 μM for $Lu(NO_3)_3$. This data is not normalized to the mass of solids used nor is it obtained for the same Ln^{3+} concentrations. See text and Table 2 for normalized energies.

Al_2O_3 phases. The pH_{PZC} values are 8.7 for γ-Al_2O_3 with 2 nm pores[43], 10.9 for porous Al_2O_3 with ~1.3 nm pores[42], and 9.7 for corundum[42]. Lanthanides are Brønsted acids and can hydrolyze water; however, pK_a values for the first hydrolysis product for the Ln^{3+} cations considered here are >7[52], thus in our experiments, Ln^{3+} cations are expected to be in the aqua-ion form $[Ln{\cdot}(H_2O)_8]^{3+}$. Therefore, the coulombic interactions at Al_2O_3 surfaces are unfavorable for adsorption and are likely more unfavorable for Nd^{3+} because of its larger solvation shell and less effective charge screening compared to Lu^{3+}. Consider hydration energies (ΔG_{hydr}) second: the ΔG_{hydr} for Nd^{3+} is lower than that of Lu^{3+}, which is then harder to de-solvate prior to inner-sphere adsorption. Consider chemical free energy changes (ΔG_{chem}) third: the Lu-O bond length is shorter by ~0.2 Å compared to Nd-O bond length (Table 1); therefore, ΔG_{chem} for Lu surface complexes at Al-OH sites is more favorable than for the analogous Nd complexes. We observed that Lu^{3+} undergoes chemisorption on both confined and unconfined surfaces, while Nd^{3+} undergoes physisorption on unconfined, and chemisorption on nanoconfined surfaces. We conclude that the ΔG_{chem} term for Lu^{3+} compensates for the more unfavorable ΔG_{hydr} contribution in both nanoconfined and unconfined systems. For Nd^{3+}, because of its lower degree of charge screening and less favorable ΔG_{chem}, physisorption dominates for unconfined surfaces. We interpret the switch from outer- to inner-sphere adsorption for Nd in nanopores to be due to ΔG_{hydr} becoming less negative due to nanoconfinement, which allows Nd^{3+} to shed 1–2 H_2O molecules prior to adsorption in nanopores. It is important to note, that *all of the considered* ΔG values are likely affected by nanoconfinement in different ways. Solvation free energies become less negative in nanopores, compared to the reported ΔG_{hydr} values[29], however, the exact change in the ΔG_{hydr} value remains unresolved. Similarly, ΔG_{coul} likely increases in nanopores because of decreased charge screening due to ΔG_{hydr} values becoming less negative. Future work is urgently needed to unravel all the important thermodynamic contributions in charged

Table 2 Summary of thermodynamic parameters calculated from batch adsorption data and measured by *operando* flow microcalorimetry experiments.

	Coverage, μmol·m^{-2}		ΔH_{ads}, kJ·mol^{-1}		ΔS_{ads}, kJ·mol^{-1}K		ΔG_{ads} at 25 C, kJ·mol^{-1}	
	CRDM	4nm-Al_2O_3	CRDM	4nm-Al_2O_3	CRDM	4nm-Al_2O_3	CRDM	4nm-Al_2O_3
Batch adsorption measurements								
Nd	0.002	70	+6	+18	+0.02	−0.02	−1	+25
Tb	0.003	211	+1	+9	+0.01	−0.04	−2	+22
Lu	0.002	505	+4	+18	+0.02	−0.01	−3	+20
Lu		102		+3		−0.07		+23
	Coverage, μmol·m^{-2}		ΔH, kJ·mol^{-1}					
	CRDM	4nm-Al_2O_3	CRDM	4nm-Al_2O_3				
Operando flow microcalorimetry measurements								
Nd	25	0.00777	+1	−55				
Tb	34	0.14578	+1	−13				
Lu	38	0.01401	+2	−35				

CRDM = corundum.

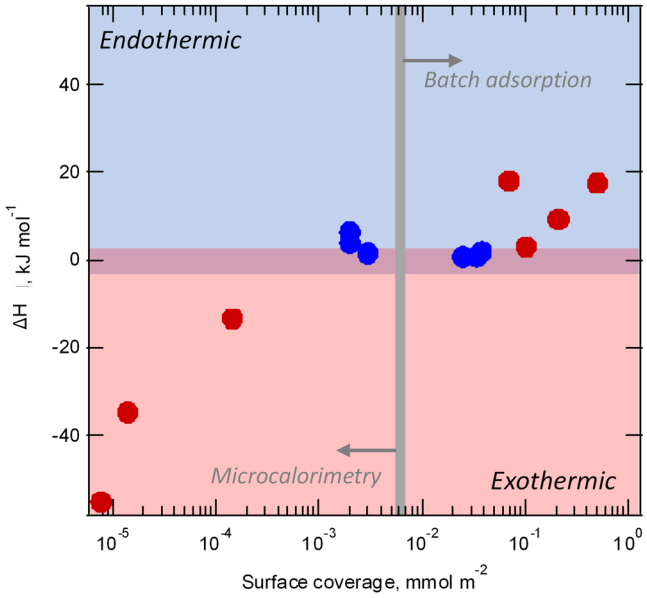

Fig. 3 All measured enthalpies plotted as a function of surface coverage. Red symbols are Al_2O_3 nanopores, blue symbols are corundum. Data at <0.001 mmol m^{-2} coverage is from microcalorimetry measurements, and data for higher surface coverages is from batch adsorption measurements.

nanopores, that control surface reactivities in important ways presented here.

Conclusions

In summary, we show that an ion's ΔG_{hydr} determines whether nanoconfinement changes the products of its adsorption and associated thermodynamics, and therefore ΔG_{hydr} can be used as a predictor. Since Nd^{3+} has less negative ΔG_{hydr} compared to Lu^{3+}, it forms different surface complexes on unconfined versus nanoconfined Al_2O_3 surfaces. The balance between an ion's (de) solvation costs, coulombic interactions, and chemical free energy change dictates whether adsorption will occur through an outer- or an inner-sphere complex. Therefore, in nanoconfined systems where the average dielectric response of water is lowered[19], inner-sphere complexation is promoted. This is because a decreased dielectric response makes Ln^{3+} ΔG_{hydr} less negative, reducing the energetic cost of the ion's partial desolvation prior to inner-sphere adsorption.

Methods

Al_2O_3 materials and temperature-controlled batch adsorption experiments. Alumina Al_2O_3 with a mean pore diameter of 4.4 ± 0.1 nm and surface area of 335 ± 2 m^2 g^{-1} (herein referred to as "nanoconfined Al_2O_3 surfaces") and non-porous corundum α-Al_2O_3 particles with a surface area of 1.5 m^2 g^{-1} were purchased from Sigma Aldrich. Lanthanide stock solutions were made from nitrate salts $Ln(NO_3)_3$ using 18 MΩ·cm Milli-Q water.

To determine enthalpy (ΔH_{ads}), entropy (ΔS_{ads}), and Gibbs free energy (ΔG_{ads}) of Ln^{3+} adsorption samples were prepared by shaking 20 ± 1 mg of dry Al_2O_3 powders in ~19 mL of 0.01 M HEPES (N-(2-Hydroxyethyl)piperazine-N′-(2-ethanesulfonic acid)) buffer solution for 1 hour prior to adding Ln^{3+}. To begin the adsorption experiment, ~1 mL of Ln^{3+} stock solution was added to each reactor to obtain a 20 mL total volume at a Ln^{3+} concentration of 0.03-0.34 μM. The pH was 6.5 ± 0.1 for all samples. Adsorption proceeded for 23 hours at controlled temperatures of 25 ± 1 °C, 35 ± 1 °C, and 45 ± 1 °C in a water bath. Samples were withdrawn while still submerged in the water bath and filtered using a 0.2 μm nylon membrane immediately, so no temperature changes occur during sampling. Samples were acidified with 6 N ultrapure HNO_3. The concentrations of each Ln^{3+} remaining in the solution after adsorption took place were quantified using inductively coupled plasma mass spectrometry (ICP-MS, NexION 350D, Perkin Elmer). Calibration curves for each analyte were obtained by running certified standard solutions prior to each analytical run, with a resulting R^2 value of 0.9999 or better. After equilibrium *Kd* values were determined from aqueous concentrations, enthalpy, and entropy values were then calculated using van't Hoff Eq. (2); and free energy was calculated using Eq. (3):

$$\ln(K_d) = \Delta S/R - \Delta H/RT \quad (2)$$

$$\Delta G = \Delta H - T\Delta S \quad (3)$$

where K_d is the equilibrium constant for a given temperature and Ln^{3+} concentration, T is the absolute temperature (K), and R is the universal gas constant (8.314 J·mol^{-1}·K^{-1}). Plotting $\ln(K_d)$ vs $1/T$ yielded straight lines for both Al_2O_3 solids and for all Ln^{3+}, and we used the slope and intercept values to estimate ΔH_{ads}, ΔS_{ads}, and ΔG_{ads}.

X-ray absorption fine structure analysis. Samples for the XAFS analyses were prepared by shaking 400 ± 5 mg of dry Al_2O_3 powders in 148 mL of 0.01 M NaCl for a minimum of 48 h. To begin the adsorption experiment, ~1 mL of Ln^{3+} stock solution was added to each reactor to obtain a 150 mL total volume at a Ln^{3+} concentration of 0.1 mM. These solutions were immediately adjusted to pH 6.0 ± 0.1 with NaOH or HCl. Throughout our experiments we chose pH 6.0 or pH 6.5 because this pH range is environmentally relevant: due to the atmospheric CO_2 dissolution into natural waters, pH between 6 and 6.5 is typical in natural systems. The second reason for choosing pH <7 is because it is below the first hydrolysis constant for lanthanides (>7), therefore the cations of interest were present as aqua-complexes with +3 charge in solution[52]. Ln^{3+}adsorption proceeded for 48 h at ambient temperature (22 °C), at which point adsorption equilibrium was reached. Samples were then centrifuged, and the supernatant was filtered using a 0.2 μm nylon membrane filter before being acidified with 6 N ultrapure HNO_3. The concentrations of each Ln^{3+} remaining in the solution after adsorption took place were quantified using ICP-MS, NexION 350D.

The remaining wet pastes from the bottom of the centrifuged reactors were stored in a refrigerator at 4 °C for XAFS spectroscopy analyses. Prior to data collection, these pastes were mounted on plastic sample holders with ~2 mm depth. XAFS data at the Nd, Tb, and Lu L_{III}-edges was collected using beamline 10-BM at the Advanced Photon Source (APS), Argonne National Laboratory. The beamline

is equipped with a water-cooled Si(111) monochromator, which was detuned by 50% to reject higher harmonics and calibrated using metal reference foils. The monochromator step size was 10 eV in the pre-edge, 0.5 eV in the XANES region, and 0.05 $Å^{-1}$ in the XAFS region. Fluorescent counts were collected using a Vortex Si Drift solid-state 4-element detector. The XAFS data were processed using the Athena interface and fitted using the Artemis interface[53] to the IFEFFIT[54] by fitting theoretical paths[55], which were based on the structures of lanthanide-containing apatite[56]. The structure files were edited to remove partial occupancies so that FEFF calculations could be performed. The background subtraction (AUTOBK algorithm[57]), normalization, and conversion into k-space were conducted as described elsewhere[58]. The fitting was done in R-space using a Hanning window and k-weights of 1, 2, and 3. R-factor cut-off of <0.05 was used to indicate a reasonable fit. In our samples, R-factors are between 0.01 and 0.02. The amplitude reduction factor (S_0) was determined by fitting XAFS spectra collected on Nd_2O_3, Tb_2O_3, and Lu_2O_3 standards; S_0 was 0.88 for Nd, 0.67 for Tb, and 0.71 for Lu. Fitting errors at a 95% confidence level (2 sigma) are shown in parenthesis in Table 1.

Flow microcalorimetry experiments. Custom flow microcalorimeter in the Kabengi Laboratory at Georgia State University[59] was used to obtain thermal signatures and subsequently, the heats of Nd^{3+}, Tb^{3+}, and Lu^{3+} ion exchange using a uniformly-packed micro-column with 20.0 ± 0.5 mg porous Al_2O_3 sample or 50.0 ± 0.5 mg of corundum particles. The packed microcolumn was equilibrated with a 0.01 M $NaNO_3$ solution at a flow rate of 0.30 ± 0.03 mL min^{-1} until a steady baseline indicative of thermal equilibrium was observed. A known mass of Ln^{3+} was injected into the column with a controlled volume of $Ln(NO_3)_3$ stock solution. The calorimetric signal corresponding to the interaction of Ln^{3+} with the Al_2O_3 surfaces was obtained following Ln^{3+} injection. Once the thermal signal returned to the original baseline, the input solution was switched back to 0.01 M $NaNO_3$. For porous Al_2O_3, the concentrations were 7.86 µM for $Nd(NO_3)_3$, 11.22 µM for $Tb(NO_3)_3$ and 8.42 µM for $Lu(NO_3)_3$. Due to the low calorimetric signal obtained for corundum, the concentrations of the stock solutions were increased to 157.2 µM for $Nd(NO_3)_3$, 224.4 µM for $Tb(NO_3)_3$, and 168.4 µM for $Lu(NO_3)_3$. Aqueous concentrations of Ln^{3+} in the column effluent samples were quantified using ICP-MS as described above. The mass of Ln^{3+} retained at (and subsequently desorbed from) the surface was determined by a mass balance calculation between the mass of the injected Ln^{3+} and the mass recovered in all effluents. The heats of reactions (Q_{ads} in mJ·m^{-2}) and molar enthalpies (ΔH_{ads} in kJ·mol^{-1}) were calculated by integrating the calorimetric peaks that were converted to energy units (Joules) by calibration with calorimetric peaks of known energy inputs generated from a calibrating resistor placed inside the microcolumn. The solution pH was adjusted daily to pH 6.0 ± 0.1 using dropwise addition of 0.1 M HNO_3 and 0.1 M NaOH. Changes in total concentration and ionic strength resulting from pH adjustments were determined to be negligible.

Data availability

The temperature-dependent adsorption data used to calculate thermodynamic values is included in the Supporting Information file (Table S1). The raw microcalorimetry and XAFS datasets generated during the current study are available from the corresponding author on reasonable request.

Received: 17 April 2023; Accepted: 8 August 2023;
Published online: 22 August 2023

References

1. Yoshitake, H., Yokoi, T. & Tatsumi, T. Adsorption behavior of arsenate at transition metal cations captured by amino-functionalized mesoporous silicas. *Chem. Mater.* **15**, 1713–1721 (2003).
2. Yang, D., Liu, H., Zheng, Z., Sarina, S. & Zhu, H. Titanate-based adsorbents for radioactive ions entrapment from water. *Nanoscale* **5**, 2232–2242 (2013).
3. Sangvanich, T. et al. Selective capture of cesium and thallium from natural waters and simulated wastes with copper ferrocyanide functionalized mesoporous silica. *J. Hazard. Mater.* **182**, 225–231 (2010).
4. Zhang, Y. et al. Unveiling the adsorption mechanism of zeolitic imidazolate framework-8 with high efficiency for removal of copper ions from aqueous solutions. *Dalton Trans.* **45**, 12653–12660 (2016).
5. Morcos, G. S., Ibrahim, A. A., El-Sayed, M. M. & El-Shall, M. S. High performance functionalized UiO metal organic frameworks for the efficient and selective adsorption of Pb (II) ions in concentrated multi-ion systems. *J. Environ. Chem. Eng.* **9**, 105191 (2021).
6. Logar, N. Z. & Kaucic, V. Nanoporous materials: from catalysis and hydrogen storage to wastewater treatment. *Acta Chim. Slov.* **53**, 117 (2006).
7. Rani, S. L. S. & Kumar, R. V. Insights on applications of low-cost ceramic membranes in wastewater treatment: a mini-review. *Case Stud. Chem. Environ. Eng.* **4**, 100149 (2021).
8. Bowen, W. R. & Welfoot, J. S. Modelling the performance of membrane nanofiltration—critical assessment and model development. *Chem. Eng. Sci.* **57**, 1121–1137 (2002).
9. Coplen, T. B. & Hanshaw, B. B. Ultrafiltration by a compacted clay membrane —I. Oxygen and hydrogen isotopic fractionation. *Geochim. et. Cosmochim. Acta* **37**, 2295–2310 (1973).
10. Epsztein, R., DuChanois, R. M., Ritt, C. L., Noy, A. & Elimelech, M. Towards single-species selectivity of membranes with subnanometre pores. *Nat. Nanotechnol.* **15**, 426–436 (2020).
11. Li, C., Sun, W., Lu, Z., Ao, X. & Li, S. Ceramic nanocomposite membranes and membrane fouling: a review. *Water Res.* **175**, 115674 (2020).
12. Wang, Y. Nanogeochemistry: nanostructures, emergent properties and their control on geochemical reactions and mass transfers. *Chem. Geol.* **378**, 1–23 (2014).
13. Ilgen, A. G. et al. Shales at all scales: exploring coupled processes in mudrocks. *Earth-Sci. Rev.* **166**, 132–152 (2017).
14. Lomba, R. F., Chenevert, M. & Sharma, M. M. The ion-selective membrane behavior of native shales. *J. Pet. Sci. Eng.* **25**, 9–23 (2000).
15. Ferreira, D., Schulthess, C. & Kabengi, N. Calorimetric evidence in support of the nanopore inner sphere enhancement theory on cation adsorption. *Soil Sci. Soc. Am. J.* **77**, 94–99 (2013).
16. Knight, A. W., Kalugin, N. G., Coker, E. & Ilgen, A. G. Water properties under nano-scale confinement. *Sci. Rep.* **9**, 8246 (2019).
17. Nelson, J., Bargar, J. R., Wasylenki, L., Brown, G. E. Jr & Maher, K. Effects of nano-confinement on Zn (II) adsorption to nanoporous silica. *Geochim. et. Cosmochimi. Acta* **240**, 80–97 (2018).
18. Wu, D. & Navrotsky, A. Small molecule–Silica interactions in porous silica structures. *Geochim. et. Cosmochim. Acta* **109**, 38–50 (2013).
19. Fumagalli, L. et al. Anomalously low dielectric constant of confined water. *Science* **360**, 1339–1342 (2018).
20. Ballenegger, V. & Hansen, J.-P. Dielectric permittivity profiles of confined polar fluids. *J. Chem. Phys.* **122**, 114711 (2005).
21. Deißenbeck, F., Freysoldt, C., Todorova, M., Neugebauer, J. & Wippermann, S. Dielectric properties of nanoconfined water: a canonical thermopotentiostat approach. *Phys. Rev. Lett.* **126**, 136803 (2021).
22. Jalali, H., Lotfi, E., Boya, R. & Neek-Amal, M. Abnormal dielectric constant of nanoconfined water between graphene layers in the presence of salt. *J. Phys. Chem. B* **125**, 1604–1610 (2021).
23. Morikawa, K., Kazoe, Y., Mawatari, K., Tsukahara, T. & Kitamori, T. Dielectric constant of liquids confined in the extended nanospace measured by a streaming potential method. *Anal. Chem.* **87**, 1475–1479 (2015).
24. Motevaselian, M. H. & Aluru, N. R. Universal reduction in dielectric response of confined fluids. *ACS Nano* **14**, 12761–12770 (2020).
25. Takei, T. et al. Changes in density and surface tension of water in silica pores. *Colloid Polym. Sci.* **278**, 475–480 (2000).
26. Le Caër, S. et al. A trapped water network in nanoporous material: the role of interfaces. *Phys. Chem. Chem. Phys.* **13**, 17658–17666 (2011).
27. Le Caër, S. et al. Dynamics in hydrated inorganic nanotubes studied by neutron scattering: towards nanoreactors in water. *Nanoscale Adv.* **3**, 789–799 (2021).
28. Baum, M., Rieutord, F., Juranyi, F., Rey, C. & Rébiscoul, D. Dynamical and structural properties of water in silica nanoconfinement: impact of pore size, ion nature, and electrolyte concentration. *Langmuir* **35**, 10780–10794 (2019).
29. Ilgen, A. G. et al. Defining silica–water interfacial chemistry under nanoconfinement using lanthanides. *Environ. Sci.: Nano* **8**, 432–443 (2021).
30. Knight, A. W. et al. Interfacial reactions of Cu (ii) adsorption and hydrolysis driven by nano-scale confinement. *Environ. Sci.: Nano* **7**, 68–80 (2020).
31. Knight, A. W., Tigges, A. & Ilgen, A. Adsorption of copper on mesoporous silica: the effect of nano-scale confinement. *Geochem. Trans.* **19**, 13 (2018).
32. Ferreira, D. & Schulthess, C. The nanopore inner sphere enhancement effect on cation adsorption: sodium, potassium, and calcium. *Soil Sci. Soc. Am. J.* **75**, 389–396 (2011).
33. Ilgen, A. G., Leung, K., Criscenti, L. J. & Greathouse, J. A. Adsorption at nanoconfined solid–water interfaces. *Ann. Rev. Phys. Chem.* **74**, 169–191 (2023).
34. Dewan, S. et al. Structure of Water at Charged Interfaces: A Molecular Dynamics Study. *Langmuir* **30**, 8056–8065 (2014).
35. Schulthess, C., Taylor, R. & Ferreira, D. The nanopore inner sphere enhancement effect on cation adsorption: sodium and nickel. *Soil Sci. Soc. Am. J.* **75**, 378–388 (2011).
36. Kim, Y., Kim, C., Choi, I., Rengaraj, S. & Yi, J. Arsenic removal using mesoporous alumina prepared via a templating method. *Environ. Sci. Technol.* **38**, 924–931 (2004).
37. Wang, Y., Bryan, C., Xu, H. & Gao, H. Nanogeochemistry: Geochemical reactions and mass transfers in nanopores. *Geology* **31**, 387–390 (2003).

38. Ilgen, A. Systems and Methods for separating rare earth elements using mesoporous materials. (2020).
39. D'Angelo, P. & Spezia, R. Hydration of lanthanoids (III) and actinoids (III): an experimental/theoretical saga. *Chem.–A Eur. J.* **18**, 11162–11178 (2012).
40. Ni, Y., Hughes, J. M. & Mariano, A. N. Crystal chemistry of the monazite and xenotime structures. *Am. Mineralogist* **80**, 21–26 (1995).
41. Zhu, Y. et al. Ionic surface propensity controls pH in nanopores. *Chem* **8**, 3081–3095 (2022).
42. Sun, Y. et al. Comparison of U (VI) removal from contaminated groundwater by nanoporous alumina and non-nanoporous alumina. *Sep. Purif. Technol.* **83**, 196–203 (2011).
43. Wang, Y. et al. Interface chemistry of nanostructured materials: Ion adsorption on mesoporous alumina. *J. Colloid Interface Sci.* **254**, 23–30 (2002).
44. Yakubovich, O., Simonov, M., Voloshin, A. & Pakhomovsky, Y. Crystal structure of keivite Yb2[Si2O7]. *Sov. Phys. Dokl.* **31**, 930–932 (1986).
45. Dardenne, K. et al. Low temperature XAFS investigation on the lutetium binding changes during the 2-line ferrihydrite alteration process. *Environ. Sci. Technol.* **36**, 5092–5099 (2002).
46. Markich, S. J. Uranium speciation and bioavailability in aquatic systems: an overview. *Sci. World J.* **2**, 707–729 (2002).
47. Majumdar, D., Roszak, S., Balasubramanian, K. & Nitsche, H. Theoretical study of aqueous uranyl carbonate (UO2CO3) and its hydrated complexes: UO2CO3· nH2O (n= 1–3). *Chem. Phys. Lett.* **372**, 232–241 (2003).
48. Allen, N., Dai, C., Hu, Y., Kubicki, J. D. & Kabengi, N. Adsorption study of Al3+, Cr3+, and Mn2+ onto quartz and corundum using flow microcalorimetry, quartz crystal microbalance, and density functional theory. *ACS Earth Space Chem.* **3**, 432–441 (2019).
49. Machesky, M. L., Bischoff, B. L. & Anderson, M. A. Calorimetric investigation of anion adsorption onto goethite. *Environ. Sci. Technol.* **23**, 580–587 (1989).
50. Falaise, C. et al. Capture of actinides (Th 4+,[UO 2] 2+) and surrogating lanthanide (Nd 3+) in porous metal–organic framework MIL-100 (Al) from water: selectivity and imaging of embedded nanoparticles. *Dalton Trans.* **46**, 12010–12014 (2017).
51. James, R. O. & Healy, T. W. Adsorption of hydrolyzable metal ions at the oxide—water interface. III. A thermodynamic model of adsorption. *J. Colloid Interface Sci.* **40**, 65–81 (1972).
52. Shiery, R. C., Cooper, K. A. & Cantu, D. C. Computational prediction of all lanthanide aqua ion acidity constants. *Inorg. Chem.* **60**, 10257–10266 (2021).
53. Ravel, B. & Newville, M. ATHENA, ARTEMIS, HEPHAESTUS: data analysis for X-ray absorption spectroscopy using IFEFFIT. *J. Synchrotron Radiat.* **12**, 537–541 (2005).
54. Newville, M. IFEFFIT: interactive XAFS analysis and FEFF fitting. *J. Synchrotron Radiat.* **8**, 322–324 (2001).
55. Zabinsky, S., Rehr, J., Ankudinov, A., Albers, R. & Eller, M. Multiple-scattering calculations of x-ray-absorption spectra. *Phys. Rev. B* **52**, 2995–3009 (1995).
56. Fleet, M. E. & Pan, Y. Site preference of rare earth elements in fluorapatite. *Am. Mineral.* **80**, 329–335 (1995).
57. Newville, M., Livins, P., Yacoby, Y., Rehr, J. & Stern, E. Near-edge x-ray-absorption fine structure of Pb: a comparison of theory and experiment. *Phys. Rev. B* **47**, 14126–14131 (1993).
58. Kelly, S., Hesterberg, D. & Ravel, B. In *Methods of Soil Analysis: Part 5--Mineralogical Methods* (eds AL Ulery & LR Drees) Ch. 14, 387–465 (Soil Science Society of America, 2008).
59. Rhue, R., Appel, C. & Kabengi, N. Measuring surface chemical properties of soil using flow calorimetry 1. *Soil Sci.* **167**, 782–790 (2002).

Acknowledgements

The authors thank Y. Ding and A.W. Knight for help during XAFS data collection, P. Ilani-Kashkouli for collecting raw microcalorimetry data, and Tuan Ho and Kevin Leung for pre-submission review of this manuscript. This work was supported by the US Department of Energy, Office of Science, Office of Basic Energy Sciences, Chemical Sciences, Geosciences and Biosciences Division under Field Work Proposal # 23-015452. X-ray Absorption Spectroscopy experiments were performed at Sector 10 at the Advanced Photon Source, an Office of Science User Facility operated for the U.S. Department of Energy (DOE) Office of Science by Argonne National Laboratory. This paper describes objective technical results and analysis. Any subjective views or opinions that might be expressed in the paper do not necessarily represent the views of the U.S. Department of Energy or the United States Government. This article has been authored by an employee of National Technology & Engineering Solutions of Sandia, LLC under Contract No. DE-NA0003525 with the U.S. Department of Energy (DOE). The employee owns all right, title and interest in and to the article and is solely responsible for its contents. The United States Government retains and the publisher, by accepting the article for publication, acknowledges that the United States Government retains a non-exclusive, paid-up, irrevocable, world-wide license to publish or reproduce the published form of this article or allow others to do so, for United States Government purposes. The DOE will provide public access to these results of federally sponsored research in accordance with the DOE Public Access Plan https://www.energy.gov/downloads/doe-public-access-plan. This paper describes objective technical results and analysis. Any subjective views or opinions that might be expressed in the paper do not necessarily represent the views of the U.S. Department of Energy or the United States Government.

Author contributions

The manuscript was written through contributions of all authors. All authors have given approval to the final version of the manuscript. AGI developed research hypothesis, prepared samples, and performed XAFS experiments and data analysis. NK designed the microcalorimetry experiments, interpreted microcalorimetry and other presented results. JGS and KMMS assisted in sample preparation and initial calculations from the controlled-temperature batch adsorption experiments.

Competing interests

The authors declare no competing interests.

Additional information

Supplementary information The online version contains supplementary material available at https://doi.org/10.1038/s42004-023-00978-3.

Correspondence and requests for materials should be addressed to Anastasia G. Ilgen.

Peer review information *Communications Chemistry* thanks Anna Romanchuk and the other, anonymous, reviewer(s) for their contribution to the peer review of this work. A peer review file is available.

Reprints and permission information is available at http://www.nature.com/reprints

Publisher's note Springer Nature remains neutral with regard to jurisdictional claims in published maps and institutional affiliations.